



1 **Enhanced hydrophobicity and volatility of submicron aerosols under**
2 **severe emission control conditions in Beijing**

3
4 **Yuying Wang¹, Fang Zhang^{1*}, Zhanqing Li^{1*}, Haobo Tan², Hanbing Xu³, Jingye**
5 **Ren¹, Jian Zhao⁴, Wei Du⁴, Yele Sun⁴**

6
7 ¹College of Global Change and Earth System Science, Beijing Normal University,
8 Beijing 100875, China

9 ²Key Laboratory of Regional Numerical Weather Prediction, Institute of Tropical and
10 Marine Meteorology, China Meteorological Administration, Guangzhou 510080,
11 China

12 ³Shared Experimental Education Center, Sun Yat-sen University, Guangzhou 510275,
13 China

14 ⁴State Key Laboratory of Atmospheric Boundary Layer Physics and Atmospheric
15 Chemistry, Institute of Atmospheric Physics, Chinese Academy of Sciences, Beijing
16 100029, China

17
18 **Correspondence to:* F. Zhang (fang.zhang@bnu.edu.cn), Z. Li (zli@atmos.umd.edu)

19
20
21
22
23
24
25
26



Abstract. A series of strict emission control measures were implemented in Beijing and the surrounding seven provinces to ensure good air quality during the 2015 China Victory Day parade, rendering a unique opportunity to investigate anthropogenic impact of aerosol properties. Submicron aerosol hygroscopicity and volatility were measured during and after the control period using a hygroscopic and volatile tandem differential mobility analyzer (H/V-TDMA) system. Three periods, namely, the control clean period (Clean1), the non-control clean period (Clean2), and the non-control pollution period (Pollution), were selected to study the effect of the emission control measures on aerosol hygroscopicity and volatility. Aerosol particles became more hydrophobic and volatile due to the emission control measures. The hygroscopicity parameter (κ) of 40–200 nm particles decreased by 32.0%–8.5% during the Clean1 period relative to the Clean2 period, while the volatile shrink factor (SF) of 40–300 nm particles decreased by 7.5%–10.5%. The emission controls also changed the diurnal variation patterns of both the probability density function of κ (κ -PDF) and the probability density function of SF (SF-PDF). During Clean1 the κ -PDF showed one nearly-hydrophobic (NH) mode for particles in the nucleation mode, which was likely due to the dramatic reduction in industrial emissions of inorganic trace gases. Compared to the Pollution period, particles observed during the Clean1 and Clean2 periods exhibited a more significant non-volatile (NV) mode throughout the day, suggesting a more externally-mixed state particularly for the 150 nm particles. Aerosol hygroscopicities increased as particle sizes increased, with the greatest increases seen during the Pollution period. Accordingly, the aerosol volatility



49 became weaker (i.e., SF increased) as particle sizes increased during the Clean1 and
50 Clean2 periods, but no apparent trend was observed during the Pollution period.
51 Based on a correlation analysis of the number fractions of NH and NV particles, we
52 found that a higher number fraction of hydrophobic and volatile particles during the
53 emission control period.

54 1. Introduction

55 China, as the world's second largest economy, is facing severe air pollution
56 problems due to its rapid economic growth. This has led to highly elevated aerosol
57 concentrations, especially in urban regions such as Beijing, Shanghai, and Guangzhou
58 (Hsu et al., 2012; Huang et al., 2014). Every year, high levels of fine particulate
59 matter (PM) have caused many severe haze days in these regions, that may pose a
60 great health hazard and changes in the regional climate because of aerosol direct and
61 indirect climate effects (Z. Li et al., 2016; G. X. Wu et al., 2016). However, the
62 climate effects of aerosols still remain highly uncertain due to the highly variable
63 physical and chemical properties of aerosols, as well as complex mechanisms that
64 govern aerosol-climate interactions (Tao et al., 2012).

65 Aerosol hygroscopicity and volatility are two important physical properties
66 describing the process of haze formation and its effects on climate. Aerosol
67 hygroscopicity describes the interaction of aerosols and water vapor under sub- and
68 supersaturation conditions, and is a vital parameter to the aerosol life cycle, aerosol
69 activation ability, and aerosol direct and indirect climate effects (Swietlicki et al.,



2008; Tao et al., 2012; Bian et al., 2014). Aerosol volatility is a physical parameter correlated with carbonaceous aerosols, commonly used to study the aerosol mixing state and aging level (Wehner et al., 2009; S. L. Zhang et al., 2016). To date, there are many ways to measure aerosol hygroscopicity and volatility, but the most popular one is the Hygroscopic and Volatile Tandem Differential Mobility Analyzer (H/V-TDMA) system because it can measure these properties in great detail (Swietlicki et al., 2008).

The Chinese government took many drastic measures to reduce the emissions of air pollutants from industry, road traffic, and construction sites, especially during some great events such as the 2008 Summer Olympic Games, the 2014 Asia-Pacific Economic Cooperation. Swift and drastic improvement in air quality (Huang et al., 2015; Shi et al., 2016) provide unique opportunities to investigate the effects of emissions on air quality. To our knowledge, previous studies have usually focused on aerosol chemistry, sources, and transport (Wang et al., 2010; Gao et al., 2011; Sun et al., 2016b), but not on the effects of emission controls on aerosol hygroscopicity and volatility. Due to the importance of the two factors on describing the process of haze formation as well as the effect on climate, it is necessary to investigate the changes in aerosol hygroscopicity and volatility when emission control measures are in place.

To guarantee good air quality in Beijing during the 2015 China Victory Day parade, the Chinese government implemented much stricter emission control measures than normally done in Beijing and the surrounding seven provinces from 20 August to 3 September. The control measures consisted of a ban on driving vehicles every other day, shutting down or limiting factory production, stopping construction



92 activities, and so on. These emission control measures successfully ensured a
93 continuous stretch of 15 days of blue sky, vividly named “Parade Blue” (H. Li et al.,
94 2016). During and after the parade emission control period, we conducted in situ
95 measurements of submicron aerosol chemical and physical properties in Beijing.
96 Size-resolved chemical compositions were also obtained (Zhao et al., 2016,
97 published). The average PM less than 1 μm in diameter (PM_{10}) concentration was 19.3
98 $\mu\text{g m}^{-3}$ during the parade emission control period, 57% lower than that after the
99 control period. All chemical species decreased during the control period, but their
100 decreasing percentages were different.

101 This study period is unique for investigating aerosol properties during low PM
102 level periods. This paper will further evaluate the impact of emission controls on the
103 hygroscopicity and volatility of submicron aerosols, which may bring some insight
104 into how to reduce pollution in the future. Furthermore, investigating aerosol
105 hygroscopicity and volatility with and without emission controls will help in
106 understanding environmental and climate changes in general. This paper is structured
107 as follows. Section 2 describes the instrumentation and data used, and section 3
108 introduces the methods to data analysis. Aerosol hygroscopicity and volatility during
109 different periods were compared and discussed in section 4. Conclusions and
110 summary are given in section 5.



111 2. Experimental methods

112 2.1. Sampling site and meteorology

113 The submicron aerosol hygroscopicity and volatility were measured in situ from
 114 26 August to 7 October 2015 using the H/VTDMA system located at the Institute of
 115 Atmospheric Physics (IAP), Chinese Academy of Sciences (39.97°N, 116.37°E),
 116 which is located between the north 3rd and 4th ring road in northern Beijing. The
 117 sampling instruments were put into a white container at ground level and an air
 118 conditioner was used to maintain the temperature at 20–25°C inside the container.
 119 Meteorological variables, including temperature (T), relative humidity (RH), wind
 120 speed (WS), and wind direction (WD), were measured at different heights of a 325 m
 121 meteorological tower, the tower located ~20 m west of the container. To eliminate the
 122 influence of buildings on wind, we selected the 280-m wind direction and 8-m wind
 123 speed as references in this study. Simultaneously, particle number concentrations (10–
 124 600 nm) were also measured by a scanning mobility particle sizer (SMPS) located at
 125 the 260-m level of the tower. The SMPS is equipped with a long differential mobility
 126 analyzer (DMA, Model 3081A, TSI Inc.) and a condensation particle counter (CPC,
 127 Model 3775, TSI Inc.). In addition, the measurement of aerosol chemical composition
 128 using a High-Resolution Aerosol Mass Spectrometer (HR-AMS) and an Aerosol
 129 Chemical Speciation Monitor (ACSM) were deployed at ground level and at the
 130 260-m level of the tower, respectively. The HR-AMS was situated in a sampling room
 131 located on the rooftop of a two-story building (~8 m), ~25 m north from the container.
 132 An analysis of the aerosol chemical composition has been done (Zhao et al., 2016,



published).

2.2. Instrumentation and operation

The H/V-TDMA system developed by the Guangzhou Institute of Tropical and Marine Meteorology (ITMM) was used to measure the submicron aerosol hygroscopicity and volatility. The H-TDMA system (H-mode) shown in Figure 1 consists of four main parts: (1) a nafion dryer (Model PD-70T-24ss, Perma Pure Inc., USA) and a bipolar neutralizer (Kr85, TSI Inc.). The nafion dryer ensured that the RH of the sample flow was below 20% over the entire measurement period, and the bipolar neutralizer was used to equilibrate the charge of particles (Wiedensohler, 1988).; (2) the first differential mobility analyzer (DMA₁, Model 3081L, TSI Inc.): The DMA₁ was used to select quasi-monodisperse particles of a certain diameter through a fixed electric voltage. The diameters selected were 40, 80, 110, 150, and 200 nm.; (3) a nafion humidifier (Model PD-70T-24ss, Perma Pure Inc., USA). The nafion humidifier was used to humidify the aerosol flow from the DMA₁ to a defined RH. In the study, we set RH to 90%.; (4) the second DMA (DMA₂, same model as the DMA₁) and a condensation particle counter (CPC, Model 3772, TSI Inc.). The DMA₂ and the CPC were used together to measure the number size distribution of the humidified particles. An automated valve located between the DMA₁ and the nafion humidifier directly connects the DMA₁ with the CPC. This can be used to measure the 10–400 nm particle number size distribution (PNSD) by varying the electric voltage of the DMA₁. Details about the design of the HTDMA system and its applications are



154 given by Tan et al. (2013a).

155 The design of the V-TDMA system (V-mode) is similar to that of the H-TDMA
156 system, except that the nafion humidifier in the V-TDMA system was replaced by a
157 heating tube that induces the evaporation of volatile materials. The heating tube was
158 an 80-cm long stainless steel tube with an inner diameter of 8 mm. With a sample
159 flow rate of 1.0 L min⁻¹, its residence time (~ 2.4 s) in the heated section is sufficient
160 for the volatile materials to be effectively vaporized (Cheung et al., 2016). In this
161 study, the heating temperature was set to 300°C. The residual particles of volatile
162 compounds at this temperature, such as sulfates, nitrates, and most organics, are
163 mainly refractory non-volatile organic carbon (such as polymer-type organics), and
164 sea salts (Philippin et al., 2004; Wehner et al., 2009; Cheung et al., 2016; Ma et al.,
165 2016). Particle were measured at the diameters of 40, 80, 110, 150, 200 and 300 nm.
166 The H/V-TDMA system has been successfully used in previous studies (Tan et al.,
167 2013b; Cheung et al., 2016; Tan et al., 2016).

168 The hygroscopic growth factor (GF) at a given RH and the volatile shrink factor
169 (SF) at a certain temperature are defined as the ratio of the conditional diameter to the
170 dry diameter, with respect to RH and T, respectively:

171
$$GF = D_p(RH)/D_{0dry}, \quad (1)$$

172
$$SF = D_p(T)/D_{0dry}. \quad (2)$$

173 Here, $D_p(RH)$ refers to the particle diameter measured at RH = 90%, $D_p(T)$ refers to
174 the particle diameter measured at T = 300°C, and D_{0dry} refers to the dry diameter set
175 by the DMA₁. The measured distribution function (MDF) versus GF or SF can be



calculated with the number concentration from CPC data downstream from the DMA₁ and the DMA₂. However, the MDF is a skewed and smoothed integral transformation of the particles' actual growth/shrink factor probability density function (GF-PDF or SF-PDF) due to the effect of the DMA diffusion transfer function (Swietlicki et al., 2008; Gysel et al., 2009). In this study, the TDMAfit algorithm (Stolzenburg et al., 1988, 2008) was used to retrieve the GF-PDF and the SF-PDF. The TDMAfit algorithm assumes that groups in the PDF following one or more lognormal distribution functions (Gaussian shape), thus allowing for the possibility that particles of a given type are not all identical.

3. Data analysis

3.1. Hygroscopicity parameter

According to the Köhler theory (Petters et al., 2007), the hygroscopicity parameter κ can be used to depict the hygroscopicity of particles at different RHs. Using H-TDMA data, κ is calculated as:

$$\kappa(\text{GF}, D_d) = (\text{GF}^3 - 1) \cdot \left[\frac{1}{\text{RH}} \exp\left(\frac{4\sigma_{s/a}M_w}{RT\rho_w D_d \text{GF}}\right) - 1 \right] \quad (3)$$

where RH is the default value of the H-TDMA, $\sigma_{s/a}$ is the surface tension of the solution/air interface, M_w is the molecular weight of water, R is the universal gas constant, T is the temperature, ρ_w is the density of water, D_d is the diameter of the dry particles (equivalent to $D_{0\text{dry}}$ as mentioned above), and GF from equation (1). In this study, T used in the κ calculation is 23°C (the average temperature of the inner container) and $\sigma_{s/a}$ is assumed to be the same as the surface tension of the pure



197 water/air interface (about 0.0723 N m^{-1} at 23°C).

198 3.2. Statistics of κ -PDF and SF-PDF

199 The probability distribution function of κ (κ -PDF, $c(\kappa, D_d)$) derived from the
 200 GF-PDF was normalized as $\int c(\kappa, D_d) d\kappa = 1$. The ensemble mean hygroscopicity
 201 parameter is then defined as the number-weighted mean GF of κ -PDF over the whole
 202 κ range:

$$203 \quad \kappa_{\text{mean}} = \int_0^\infty \kappa c(\kappa, D_d) d\kappa \quad . \quad (4)$$

204 The standard deviation of κ -PDF is:

$$205 \quad \sigma_{\kappa\text{-PDF}} = \left(\int_0^\infty (\kappa - \kappa_{\text{mean}})^2 c(\kappa, D_d) d\kappa \right)^{\frac{1}{2}} \quad . \quad (5)$$

206 The calculated statistical parameters of SF-PDF ($c(\text{SF}, D_d)$) are similar to those of
 207 κ -PDF, so SF can be used instead of κ and $c(\text{SF}, D_d)$ instead of $c(\kappa, D_d)$ in these
 208 equations.

209 3.3. Classification of different hygroscopic and volatile groups

210 The mixing state of ambient aerosol particles is complex due to different sources,
 211 different aging processes, and so on. Different hygroscopic and volatile groups had
 212 been used around the Beijing region using H-TDMAs and V-TDMAs (Massling et al.,
 213 2009; Liu et al., 2011; S. L. Zhang et al., 2016). Based on previous studies and our
 214 measurements (Figure S1), ambient aerosol particles were classified into three
 215 hygroscopic groups and three volatile groups, where κ and SF are used here to define
 216 the boundaries for each group:

217 Nearly-Hydrophobic, NH: $\kappa < 0.1$;



218 Less-Hygroscopic, LH: $0.1 \leq \kappa < 0.2$;

219 More-Hygroscopic, MH: $0.2 \leq \kappa$;

220 Non-Volatile, NV: $SF \geq 0.88$;

221 Slight-Volatile, SV: $0.88 > SF \geq 0.55$;

222 Very-Volatile, VV: $SF < 0.55$.

223 The number fraction (NF) for each hygroscopic group with the boundary of [a, b]
 224 is defined as:

$$225 \quad NF = \int_a^b c(\kappa, D_p) d\kappa \quad . \quad (6)$$

226 The number fraction of each volatile group also can be calculated using a similar
 227 equation.

228 4. Results and discussion

229 4.1. Overview of measurements

230 4.1.1. Meteorological conditions during the sampling period

231 Air quality has a strong correlation with local wind direction in Beijing. Previous
 232 studies have shown that high PM concentrations usually correspond to southerly
 233 winds, while low PM concentration are generally related to northerly winds, because
 234 there were more high concentration air pollutants from source locations south of the
 235 Beijing area (Wehner et al., 2008; Wang et al., 2010; Gao et al., 2011). Figure 2
 236 displays time series of WD at 280 m, WS at 8 m, ambient T, and RH. During the
 237 emission control period, the prevailing winds were northerly, except for the period
 238 from 29 August to 30 August due to the influence of accumulated precipitation.



239 During the non-control period, the prevailing winds changed due to the influence of
240 weather systems. Two cold fronts passed through on two different days, i.e., on the
241 night of 9 September and in the early morning of 30 September. During these frontal
242 passages, the prevailing winds were northerly, but on other days, the prevailing winds
243 were southerly and the meteorological parameters showed obvious diurnal cycle
244 patterns. Over the measurement period, the average ambient T and RH were 21.9°C
245 and 62.4%, respectively.

246 **4.1.2. Time series of κ -PDF and SF-PDF, and the division of clean and pollution** 247 **periods**

248 Figure 3 shows the time series of 10-400 nm particle mass concentrations (ρ_{10-400}
249 nm) derived from PNSD measurements and the time series of κ -PDF and SF-PDF with
250 40 nm and 150 nm particles as examples. Particles with D_p equal to 40 nm represent
251 fresh particles and particles with D_p equal to 150 nm represent pre-existing particles.
252 Several haze events during the non-control period can be seen from the time series of
253 ρ_{10-400} nm, which shows the rapid accumulation of particle mass concentration. Based
254 on mass concentrations and weather conditions, we selected several clean and
255 pollution periods to study the differences in aerosol hygroscopicity and volatility for
256 two different cases (Figure 3). To further study the effect of emission controls, we
257 divided the clean period into two periods: Clean1 (control clean period) and Clean2
258 (non-control clean period). During the Clean1, Clean2, and Pollution periods, the
259 average ρ_{10-400} nm was 6.9 ± 2.8 , 6.0 ± 4.2 , and 51.0 ± 25.6 $\mu\text{g m}^{-3}$, respectively. There was
260 no significant precipitation during the three selected periods. The time series of



261 κ -PDF and SF-PDF (Figure 3b-e) showed evident changes and fluctuations in the
262 measurements. The prominent differences in κ -PDF and SF-PDF during the three
263 periods will be discussed in the following sections.

264 A wind rose diagram (Figure S2) was used to compare winds during the different
265 periods. During the Clean1 and Clean2 periods, wind directions were similar, mainly
266 from the north and northwest. During the Pollution period, the wind direction had the
267 characteristics of mountain-valley breezes where the wind direction changed routinely
268 at midnight and changed the wind direction from southerly to northerly (Figure 2).
269 The change in wind direction at night would reduce pollution in the short term (Sun et
270 al., 2016b). Even so, the prevailing wind direction was southerly during the Pollution
271 period (Figure S2), which was favorable for the transport of pollutants from the more
272 populated and more industrialized south and southeast to Beijing. The mean WS and
273 RH were similar during all periods, but the mean temperature during the Clean2
274 period was lower than during the other periods due to the influence of cold fronts
275 (Table S1). In summary, the meteorological parameters of the Clean1 and Clean2
276 cases were similar expect for the ambient T. This provided the opportunity to compare
277 the differences in aerosol properties between control and non-control periods. The
278 high level of PM during the Pollution case can also provide a good opportunity to
279 compare differences between clean and polluted environments.



280 4.2. Diurnal variation

281 4.2.1. Diurnal variation in the aerosol size distribution

282 Figure 4a shows the diurnal variation in total number concentration of 10–400 nm
283 particles ($N_{10-400\text{ nm}}$). In general, $N_{10-400\text{ nm}}$ is higher at night and lower during the day
284 due to the influence of changes in the planetary boundary layer (PBL). However, a
285 significant peak in $N_{10-400\text{ nm}}$ is also seen at noontime because of new particle
286 formation (NPF) events (Figure S3). NPF started at about 0900 local time (LT) during
287 the Clean1 and Clean2 periods. During the Clean1 period, the $N_{10-400\text{ nm}}$ peak was
288 lower than that observed during the Clean2 period, and the peak in the Clean1 case
289 appeared two hours earlier than that in the Clean2 case (1200 LT during Clean1 and
290 1400 LT during Clean2). This illustrates that the strength of the NPF was weaker
291 during the Clean1 period than during the Clean2 period, and that it was likely related
292 to the decrease in precursors during the Clean1 period. H. Li et al. (2016) have
293 reported that during the parade control period, the precursors SO_2 , NO_x , and volatile
294 organic compounds (VOCs) decreased by 36.5%, 49.9%, and 32.4%, respectively.
295 The relatively higher ambient temperature during the Clean1 period was also
296 unfavorable for NPF (Kulmala et al., 2004).

297 Figure 4b compares diurnal variations in total mass concentration of 10–400 nm
298 particles ($\rho_{10-400\text{ nm}}$) during the three periods. No clear increase in $\rho_{10-400\text{ nm}}$ is seen
299 while $N_{10-400\text{ nm}}$ sharply increases during the Clean1 and Clean2 daytime periods. This
300 is because the D_p for most particles was less than 100 nm, which contributed little to
301 $\rho_{10-400\text{ nm}}$. During the Clean1 and Clean2 periods, $\rho_{10-400\text{ nm}}$ had an obvious diurnal



variation, which could be attributed to the evolution of the PBL. As is known, the lower PBL at night aids in the accumulation of pollutants (Achtert et al., 2009). However, this effect was weak in the pollution case because of the change in wind direction from southerly to northerly at midnight, which could partly offset the influence of the PBL.

4.2.2. Diurnal variation in aerosol hygroscopicity

Figure 5a shows the diurnal variation in size-resolved κ_{mean} during the three periods. κ_{mean} shows a peak during daytime, and is always higher than that observed during nighttime. This is because more highly aged particles due to photochemical reactions cause the increase in κ_{mean} during daytime. In the evening, a number of low hygroscopic primary particles (like black carbon, BC) emitted from local diesel trucks and heavy-duty vehicles results in the decrease in κ_{mean} during nighttime (Liu et al., 2011; S. L. Zhang et al., 2016). During the Clean2 period, there is another obvious peak at about 0300 LT in the early morning, likely related to the increase in nitrate. Because there was a large amount of NO_x emitted from traffic sources in the evening during the non-control period, with the PBL height reduction and ambient temperature decrease, NO_x could be transformed into hydrophilic nitrate through heterogeneous reactions with dissolved H_2O_2 during nighttime (Seinfeld et al., 2016). This was also verified from comparisons of the nitrate diurnal cycle with and without emission controls (Zhao et al., 2016, published).

Figure 5b shows the diurnal variation in κ -PDF for particles with D_p equal to 40



323 nm (i.e., newly-formed particles) during the three periods. During the Clean1 period,
324 the κ -PDF has a quasi-unimodal shape (only in the hydrophobic mode). During NPF
325 events, κ_{mean} increases slightly, indicating that a very small amount of hydrophilic
326 particles were produced through the nucleation and growth from gaseous precursors.
327 This is likely because the secondary formation of hydrophilic sulfate and nitrate was
328 suppressed due to low concentrations of SO_2 and NO_x during the parade control
329 period (H. Li et al., 2016). Most of the new particles should consist of less
330 hygroscopic organics that are formed by oxidation and condensation of VOCs. By
331 contrast, during the Clean2 period, the κ -PDF with D_p of 40 nm shows either a
332 bimodal or quasi-trimodal distribution and exhibits a large diurnal variation during the
333 day. Interestingly, when the NPF event occurred at about 0900 LT, the number
334 fraction of the hydrophobic mode quickly decreased and the hydrophilic mode
335 increased (Figure 5b), suggesting the conversion of externally mixed particles to
336 internally mixed particles due to the condensation of gas precursors (including SO_2 ,
337 NO_x , as well as VOCs). A similar phenomenon was also observed by Z.J. Wu et al.
338 (2016). For the Clean1 case, much less of these gases were in the atmosphere due to
339 the emission control. Around 1700 LT, the fraction of hydrophobic mode particles
340 increased again, mainly due to substantial traffic emissions at rush hour. However,
341 during the Pollution period, the κ -PDF shows a bimodal shape during the day. The
342 hydrophilic mode becomes stronger in the early morning and in the afternoon, which
343 is attributed to the NO_x heterogeneous reactions at night, and the aging and growth of
344 pre-existing particles during the day.



345 In summary, the diurnal variations in κ -PDF for 40-nm particles were
346 significantly different during the three periods and the emission control appeared to
347 change the diurnal pattern of κ -PDF, mainly due to the decrease in gas precursors, like
348 SO_2 and NO_x , the reduction of which will suppress the formation of hydrophilic
349 matter.

350 However, the κ -PDF for 150-nm D_p particles (i.e., pre-existing particles) had a
351 similar diurnal variation pattern during the three periods (Figure 5c) and showed NH
352 and MH modes. The number fraction of the MH mode increased significantly during
353 daytime. There are different reasons for the diurnal variations. One reason is that
354 during daytime, strong photochemistry can produce a large number of condensable
355 vapors, such as sulfuric acid and secondary organic species, which can condense onto
356 pre-existing particles and enhance their water absorbing capacity (Z. J. Wu et al.,
357 2016). Another reason is that when the sun rises, the PBL height increases and older
358 particles are well-mixed, making them more hydrophilic (S. L. Zhang et al., 2016).
359 However, the MH mode is much more evident for the Pollution case and may be
360 related to the higher mass fractions of inorganic salts and more internal-mixed
361 particles during the Pollution period.

362 4.2.3. Diurnal variation in aerosol volatility

363 Figure 6a shows the diurnal variation in SF_{mean} , which shows similar trends for all
364 three cases, with the lowest SF_{mean} in the afternoon (1200–1500 LT) and the highest
365 SF_{mean} in the morning (0700–0900 LT) for all particles with D_p ranging from 40–300



366 nm. The diurnal variations illustrate that particles had a higher volatility during the
367 day than at night. This feature is more obvious for those small particles observed
368 during the Clean1 period. During the Clean1 period, particle volatility increased
369 dramatically (i.e., SF_{mean} decreased) along with the occurrence of NPF events,
370 suggesting that the earliest newly-formed matter (before ~1200 LT) were always
371 volatile at 300°C. As stated previously, during the Clean1 period and likely due to the
372 dramatic reduction in soot particles, the primary emissions were VOCs from motor
373 vehicles in urban Beijing. This would lead to more VOC-formed organic particles,
374 which are normally highly volatile. Therefore, the highest volatility was observed
375 during the Clean1 period. Wehner et al. (2009) also showed that ~97% of
376 newly-formed particles are volatile because they are dominated by sulfate and VOCs.
377 With the processes of particle aging, collision, and growth, they then decrease in
378 volatility (i.e., SF_{mean} increases).

379 For 40-nm particles, the lowest SF_{mean} appeared two hours later during the Clean2
380 period (~1500 LT) than during the Clean1 period (~1300 LT). This is probably
381 because NPF lasted longer during the Clean2 period. For larger particles, the coating
382 effect of condensable vapors onto pre-existing particles was the major reason behind
383 the intensification of their volatility during NPF events (Wehner et al., 2009; Cheung
384 et al., 2016). The SF_{mean} decreased little compared to that for 40-nm particles. By
385 comparison, the diurnal variation in SF_{mean} for 40-nm particles during the Pollution
386 period changed more smoothly, likely because under a polluted environment, the mass
387 fractions of all chemical species were relatively stable (Sun et al., 2016a) and the



388 particles were well-mixed with highly aging levels.

389 Figure 6b and 6c show the diurnal variation in SF-PDF for 40 nm and 150 nm
390 particles. The SF-PDF normally has an NV mode and a SV or VV mode. The NV
391 mode consists of non-volatile particles, like BC particles, which do not shrink when
392 aerosols are heated. SV and VV modes suggest a mixture of volatile (e.g., organics)
393 and non-volatile matter that shrink when aerosols are heated (Kuhn et al., 2005). The
394 two SF-PDF modes suggest that the particles during the observed periods were mostly
395 externally-mixed. The 40-nm and 150-nm SF-PDF show similar diurnal patterns.
396 During daytime, active aging processes facilitated the mixing of primary particles
397 with secondary species, leading to the transformation of externally-mixed particles to
398 internally-mixed particles, and weakening the NV mode. In particular, this effect was
399 stronger during the Clean1 period than during the other periods. This may be due to
400 the reduction in emissions of soot particles during the control period. In the evening
401 and the early morning, the number fraction of NV-mode particles increased again
402 because a large amount of refractory particles (like BC) were emitted from traffic
403 sources or cooking, and then accumulated in the nocturnal boundary layer (S. L.
404 Zhang et al., 2016). The number fraction of NV-mode 150-nm particles in the Clean1
405 case had a stronger increase than that of 40-nm particles in the evening and early
406 morning. This is because freshly emitted refractory particles (like BC) are primarily
407 within the 150 nm to 240 nm diameter range (Levy et al., 2013). Furthermore,
408 compared with the Pollution case, the number fraction of NV-mode 150-nm particles
409 are much higher during the Clean1 and Clean2 cases. This may reflect the fact that



410 soot particles in a polluted environment can be coated and aged quickly through the
411 heterogeneous reactions of VOCs and other precursor gases (like SO₂, NO_x), which
412 are usually present in extremely high concentrations during polluted days in urban
413 Beijing (Guo et al., 2014; Sun et al., 2016a).

414 Overall, the diurnal variation in aerosol volatility is different between clean and
415 polluted periods. NPF can enhance volatility through the formation of volatile matter
416 and the coating effect of condensation vapors. Particles observed during the control
417 period showed two significant NV and VV modes during the day, suggesting a more
418 externally-mixed state, particularly for the larger particles.

419 **4.3. Size-resolved particle hygroscopic and volatile properties**

420 Table 1 summarizes the size-resolved mean κ , the growth spread factor ($\sigma_{\kappa\text{-PDF}}$) of
421 $\kappa\text{-PDF}$, size-resolved SF during different periods, and the change in percentages of κ
422 and SF due to the emission control policy. The $\sigma_{\kappa\text{-PDF}}$, defined as the standard
423 deviation of $\kappa\text{-PDF}$, is an indication of the mixing state of aerosol particles. A higher
424 $\sigma_{\kappa\text{-PDF}}$ generally suggests a higher degree of external mixing (Sjogren et al., 2008; Liu
425 et al., 2011; Jiang et al., 2016). Liu et al. (2011) chose $\sigma_{\kappa\text{-PDF}} = 0.08$ as the cut-off
426 point for high external mixing and quasi-internal mixing. In this study, $\sigma_{\kappa\text{-PDF}}$ always
427 exceeds 0.08, indicating that the particle population was more externally mixed in
428 urban Beijing. However, the mean $\sigma_{\kappa\text{-PDF}}$ of 40-nm particles during the Clean1 period
429 is equal to 0.08, suggesting that during the control period, 40-nm particles had a low
430 degree of external mixing. This is also seen in the quasi-unimodal distribution of



431 40-nm κ -PDF (Figure 5b).

432 During the selected three periods, aerosol particles were more hygroscopic (i.e., κ
433 increased) with increase in particle size (Figure 7a). The most significant trend is seen
434 in the Pollution case where κ increases from 0.16 to 0.42 when D_p changes from 40
435 nm to 200 nm, but only increases from 0.10 to 0.25 for the Clean1 case and from 0.14
436 to 0.28 for the Clean2 case. This is because particles with a larger size are usually
437 composed of more inorganic salts or oxidized organics, especially in a polluted
438 environment (Swietlicki et al., 2008; Achtert et al., 2009; Fors et al., 2011; Sun et al.,
439 2016a). Meanwhile, the increase in $\sigma_{\kappa\text{-PDF}}$ with the increase in particle size illustrates
440 that there were more external mixing particles with larger sizes (Table 1). Accordingly,
441 aerosol volatility became weaker (SF increased) as particle size increased during the
442 Clean1 and Clean2 periods, but no apparent trend was observed for the Pollution
443 period (Figure 7b). This finding is consistent with that reported by Wehner et al.
444 (2009).

445 Figure 6 also shows that all particles were less hygroscopic and more volatile
446 during the control Clean1 period than during the non-control Clean2 period, which
447 can also be seen from the variation in chemical composition. Based on HR-AMS
448 measurements, secondary inorganic aerosols (SIA) had larger decreases than organic
449 aerosols (OA) during the parade control period. The positive matrix factorization of
450 OA further illustrates that primary OA (POA) had similar decreases as secondary OA
451 (SOA). However, more-oxidized SOA had larger decreases than less-oxidized SOA
452 (Zhao et al., 2016, published). SIA is always more hydrophilic than OA and



453 more-oxidized SOA is also more hydrophilic than less-oxidized SOA (Jimenez et al.,
454 2009; Chang et al., 2010; Rickards et al., 2013; Zhang et al., 2014; F. Zhang et al.,
455 2016). Therefore, the increased fraction of POA emissions, but weakened age
456 processing due to a sharp reduction in SO₂ and NO_x, lead to particles being less
457 hygroscopic during the control period. Meanwhile, particles become relatively more
458 volatile due to the high number of POA particles because OA volatility is generally
459 inversely corrected with the O:C ratio (an indicator of oxidation state) (Jimenez et al.,
460 2009).

461 To quantify the effects of emission control on aerosol hygroscopicity and
462 volatility, Table 1 also gives the change in percentages of κ and SF during the control
463 Clean1 period compared with that during the non-control Clean2 period. Results show
464 that κ decreased by 32.0–8.5% from 40 nm to 200 nm during the control period, with
465 a more significant reduction for small particles, while SF reduced by 7.5–10.5% from
466 40 nm to 300 nm. The significant decrease in aerosol hygroscopicity is favorable for
467 decreasing the aerosol water content, thus suppressing the evolution of regional air
468 pollution (like liquid-phase chemical reaction processes in the atmosphere) (Arellanes
469 et al., 2006; Bian et al., 2014), and eventually improving atmospheric visibility.

470 In addition, because of the reduced hygroscopicity, fewer particles would be
471 activated as cloud condensation nuclei, which is a critical parameter in evaluating the
472 aerosol indirect effect. Thus, our study is important for investigating environmental
473 and climate changes, and should inspire both scientists and policy makers to think
474 more deeply about the issue of heavy air pollution in China.



4.4. Relationship between nearly-hydrophobic and non-volatile particles

For submicron particles, non-volatile (NV) particles at 300°C were normally the major nearly-hydrophobic (NH) particles because both their main components are soot particles (Massling et al., 2009; Wehner et al., 2009). S. L. Zhang et al. (2016) compared the relationship between the number fraction of measured non-volatile particles (NF_{NV}) and nearly hydrophobic (NF_{NH}) particles and found those two groups are very likely to be dominated by the same component. In this study, we also analyze the relationship of NF_{NH} and NF_{NV} particles as shown in Figure 8.

The results show that Aitken mode particles (40 nm and 80 nm) have a very weak linear relationship between NF_{NH} and NF_{NV} , likely because Aitken mode particles are not as aged. There are a large number of hydrophobic, but volatile, particles such as POA and less-oxidized SOA. Accumulation mode particles (> 100 nm) show a relatively better linear correlation between NF_{NH} and NF_{NV} , i.e., correlation coefficients (R^2) are 0.26, 0.55, and 0.62 for 110, 150, and 200 nm particles, respectively. The higher R^2 for the larger particles may arise because larger particles are highly aged particles from cloud processes. Also, freshly emitted refractory and hydrophobic matter is mostly in the accumulation mode (Levy et al., 2013). The best-fit regression line for the accumulation mode particles is always lower than the 1:1 line. This can be attributed not only to externally mixed SIA and volatile organics (completely volatile), which are not taken into account for calculation, but also to that some medium/high volatile organics are



497 nearly-hydrophobic.

498 There were obvious differences in NF_{NH} and NF_{NV} during the three selected
499 periods. For the Clean1 and Clean2 cases, NF_{NH} and NF_{NV} were larger than those
500 obtained for the Pollution case, but more scatter was seen. This is likely related to the
501 influence of NPF events, during which secondary aerosol material had more complex
502 chemical compositions due to the different sources of precursors. A higher
503 NF_{NH}/NF_{NV} ratio was seen during the Clean1 period than during the other two
504 periods, illustrating that a higher number fraction of hydrophobic and volatile
505 particles during the control period.

506

507 5. Conclusions and Summary

508 In this study, a H/V-TDMA system was used to measure submicron aerosol
509 hygroscopic and volatile properties in Beijing during and after the parade emission
510 control period. Three periods, namely, the control clean period (Clean1), the
511 non-control clean period (Clean2), and the non-control pollution period (Pollution),
512 were selected to study the effect of emission control on aerosol hygroscopicity and
513 volatility.

514 When emission control measures were in place, particles became more
515 hydrophobic and volatile compared to particles in the non-control period. The κ of
516 40–200 nm particles decreased by 32.0–8.5% during the Clean1 period relative to the
517 Clean2 period, while SF of 40–300 nm particles decreased by 7.5–10.5%. The diurnal



518 variations of κ -PDF were significantly different during the three selected periods,
519 especially for small particles. During the Clean1 period, the κ -PDF of 40-nm particles
520 always showed a quasi-unimodal distribution and had a weaker diurnal variation than
521 that observed during the Clean2 period. This demonstrates that emission control
522 measures can change the diurnal variation pattern of κ -PDF due to the reduction in
523 gas precursors like SO_2 and NO_x , which suppresses the formation of hydrophilic
524 matter. The diurnal variation in aerosol volatility was different between clean and
525 polluted periods. NPF appears to enhance aerosol volatility through the formation of
526 volatile matter and the coating effect of condensable vapors. The particles observed
527 during the control period showed two significant modes during the day, i.e., NV and
528 VV modes, and a more externally-mixed state particularly for larger particles.

529 Aerosol particles became more hygroscopic (i.e., κ increases) as the particle size
530 increased during the three periods. The trend was greatest for the Pollution case where
531 κ increased from 0.16 to 0.42 when D_p changed from 40 nm to 200 nm, but only
532 increased from 0.10 to 0.25 for the Clean1 case and from 0.14 to 0.28 for the Clean2
533 case. Meanwhile, the increase in $\sigma_{\kappa\text{-PDF}}$ (i.e., the standard deviation of κ -PDF) with the
534 increase in particle size also illustrates that there were more external mixing particles
535 with larger sizes. Accordingly, aerosol volatility became weaker (SF increased) as
536 particle size increased during the Clean1 and Clean2 periods, but no apparent trend
537 was observed for the Pollution period.

538 Our results suggest that emission control measures weaken submicron aerosol
539 hygroscopicity, and that aerosol particles are more hygroscopic in a polluted



environment. The significant decrease in aerosol hygroscopicity is favorable for suppressing the evolution of regional air pollution. In addition, because of the reduced hygroscopicity, fewer particles would be activated as could condensation nuclei, which is a critical parameter in evaluating the aerosol indirect effect. Thus, our study is important for investigating environmental and climate changes, and should inspire both scientists and policy makers to think more deeply about the issue of heavy air pollution in China from a broader perspective.

547

548 Acknowledgements

This work was funded by the NSFC research project (Grant No. 41675141, 91544217, 41375156), the National Basic Research Program of China ‘973’ (Grant No. 2013CB955800), and the NSFC-TAMU Collaborative Research Grant Program (Grant No. 4141101031). We also thank all participants in the field campaign for their tireless work and co-operation.

554

555 References

- Achtert P., Birmili W., Nowak A., Wehner B., Wiedensohler A., Takegawa N., Kondo Y., Miyazaki Y., Hu M. and Zhu T.: Hygroscopic growth of tropospheric particle number size distributions over the North China Plain, *J. Geophys. Res.*, 114, 10.1029/2008jd010921, 2009.
- Arellanes C., Paulson S.E., Fine P.M. and Sioutas C.: Exceeding of Henry's Law by Hydrogen Peroxide Associated with Urban Aerosols, *Environ. Sci. Technol.*, 40, 4859-66, 2006.
- Bian Y.X., Zhao C.S., Ma N., Chen J. and Xu W.Y.: A study of aerosol liquid water content based on hygroscopicity measurements at high relative humidity in the North China Plain, *Atmos. Chem. Phys.*, 14, 6417-6426, 2014.
- Chang R., Slowik J.G., Shantz N.C., Vlasenko A., Liggio J., Sjostedt S.J., Leaitch W.R. and Abbatt J.: The hygroscopicity parameter (κ) of ambient organic aerosol at a field site subject to biogenic and anthropogenic influences: relationship to degree of aerosol oxidation, *Atmos. Chem. Phys.*, 10, 5047-5064, 2010.
- Cheung H.H., Tan H., Xu H., Li F., Wu C., Yu J.Z. and Chan C.K.: Measurements of non-volatile



- 569 aerosols with a VTDMA and their correlations with carbonaceous aerosols in Guangzhou, China,
570 Atmos. Chem. Phys., 16, 8431-8446, 2016.
- 571 Fors E.O., Swietlicki E., Svenningsson B. and Kristensson A.: Hygroscopic properties of the ambient
572 aerosol in southern Sweden – a two year study, Atmos. Chem. Phys., 11, 8343-8361, 2011.
- 573 Gao Y., Liu X., Zhao C. and Zhang M.: Emission controls versus meteorological conditions in
574 determining aerosol concentrations in Beijing during the 2008 Olympic Games, Atmos. Chem. Phys.,
575 11, 12437-12451, 2011.
- 576 Guo S., Hu M., Zamora M.L., Peng J., Shang D., Zheng J., Du Z., Wu Z., Shao M., Zeng L., Molina
577 M.J. and Zhang R.: Elucidating severe urban haze formation in China, Proc Natl Acad Sci U S A,
578 111, 17373-8, 10.1073/pnas.1419604111, 2014.
- 579 Gysel M., McFiggans G.B. and Coe H.: Inversion of tandem differential mobility analyser (TDMA)
580 measurements, J. Aerosol Sci., 40, 134-151, 10.1016/j.jaerosci.2008.07.013, 2009.
- 581 Hsu N.C., Gautam R., Sayer A.M., Bettenhausen C., Li C., Jeong M.J., Tsay S.C. and Holben B.N.:
582 Global and regional trends of aerosol optical depth over land and ocean using SeaWiFS
583 measurements from 1997 to 2010, Atmos. Chem. Phys., 12, 8037-8053, 10.5194/acp-12-8037-2012,
584 2012.
- 585 Huang K., Zhang X. and Lin Y.: The “APEC Blue” phenomenon: Regional emission control effects
586 observed from space, Atmos. Res., 164-165, 65-75, 2015.
- 587 Huang R., Zhang Y., Bozzetti C., Ho K., Cao J., Han Y., Daellenbach K.R., Slowik J.G., Platt S.M.,
588 Canonaco F., Zotter P., Wolf R., Pieber S.M., Brunts E.A., Crippa M., Ciarelli G., Piazzalunga A.,
589 Schwikowski M., Abbaszade G., Schnelle-Kreis J., Zimmermann R., An Z., Szidat S., Baltensperger
590 U., Haddad I.E. and Prévôt A.S.H.: High secondary aerosol contribution to particulate pollution
591 during haze events in China, Nature, 10.1038/nature13774, 2014.
- 592 Jiang R.X., Tan H.B., Tang L.L., Cai M.F., Yin Y., Li F., Liu L., Xu H.B., Chan P.W., Deng X.J. and
593 Wu D.: Comparison of aerosol hygroscopicity and mixing state between winter and summer seasons
594 in Pearl River Delta region, China, Atmos. Res., 169, 160-170, 2016.
- 595 Jimenez J.L., Canagaratna M.R., Donahue N.M., Prevot A., Zhang Q., Kroll J.H., DeCarlo P.F., Allan
596 J.D., Coe H. and Ng N.L.: Evolution of organic aerosols in the atmosphere, Science, 326, 1525-1529,
597 2009.
- 598 Kuhn T., Biswas S. and Sioutas C.: Diurnal and seasonal characteristics of particle volatility and
599 chemical composition in the vicinity of a light-duty vehicle freeway, Atmos. Environ., 39,
600 7154-7166, 10.1016/j.atmosenv.2005.08.025, 2005.
- 601 Kulmala M., Vehkamäki H., Petäjä T., Dal Maso M., Lauri A., Kerminen V.M., Birmili W. and
602 McMurry P.H.: Formation and growth rates of ultrafine atmospheric particles: a review of
603 observations, J. Aerosol Sci., 35, 143-176, 10.1016/j.jaerosci.2003.10.003, 2004.
- 604 Levy M.E., Zhang R., Khalizov A.F., Zheng J., Collins D.R., Glen C.R., Yuan W., Yu X.Y., Winston L.
605 and Jayne J.T.: Measurements of submicron aerosols in Houston, Texas during the 2009 SHARP
606 field campaign, Journal of Geophysical Research Atmospheres, 118, 10518-10534, 2013.
- 607 Li H., Zhang Q., Duan F., Zheng B. and He K.: The “Parade Blue”: effects of short-term emission
608 control on aerosol chemistry., Faraday Discuss., 2016.
- 609 Li Z., Lau W.M., Ramanathan V., Wu G., Ding Y., Manoj M.G., Liu J., Qian Y., Li J. and Zhou T.:
610 Aerosol and monsoon climate interactions over Asia, Rev. Geophys., 2016.
- 611 Liu P.F., Zhao C.S., Bel T.G., Hallbauer E., Nowak A., Ran L., Xu W.Y., Deng Z.Z., Ma N.,
612 Mildnerberger K., Henning S., Stratmann F. and Wiedensohler A.: Hygroscopic properties of aerosol



- 613 particles at high relative humidity and their diurnal variations in the North China Plain, Atmos.
614 Chem. Phys., 2011.
- 615 Ma N., Zhao C., Tao J., Wu Z., Kecorius S., Wang Z., Groess J., Liu H., Bian Y., Kuang Y., Teich M.,
616 Spindler G., Mueller K., van Pinxteren D., Herrmann H., Hu M. and Wiedensohler A.: Variation of
617 CCN activity during new particle formation events in the North China Plain, Atmos. Chem. Phys.,
618 16, 8593-8607, 10.5194/acp-16-8593-2016, 2016.
- 619 Massling A., Stock M., Wehner B., Wu Z.J., Hu M., Brüggemann E., Gnauk T., Herrmann H. and
620 Wiedensohler A.: Size segregated water uptake of the urban submicrometer aerosol in Beijing,
621 Atmos. Environ., 43, 1578-1589, 2009.
- 622 Petters M.D. and Kreidenweis S.M.: A single parameter representation of hygroscopic growth and
623 cloud
624 condensation nucleus activity, Atmos. Chem. Phys., 7, 1961-1971, 2007.
- 625 Philippin S., Wiedensohler A. and Stratmann F.: Measurements of non-volatile fractions of pollution
626 aerosols with an eight-tube volatility tandem differential mobility analyzer (VTDMA-8), J. Aerosol
627 Sci., 35, 185-203, 2004.
- 628 Rickards A.M.J., Miles R.E.H., Davies J.F., Marshall F.H. and Reid J.P.: Measurements of the
629 sensitivity of aerosol hygroscopicity and the κ parameter to the O/C ratio., J. Phys. Chem. A, 117,
630 14120-31, 2013.
- 631 Seinfeld J.H. and Pandis S.N.: Atmospheric chemistry and physics: from air pollution to climate
632 change, John Wiley & Sons, 2016.
- 633 Shi H., Wang Y., Chen J. and Huisingh D.: Preventing smog crises in China and globally, J. Clean.
634 Prod., 112, 1261-1271, 2016.
- 635 Sjogren S., Gysel M., Weingartner E., Alfarra M.R., Duplissy J., Cozic J., Crosier J., Coe H. and
636 Baltensperger U.: Hygroscopicity of the submicrometer aerosol at the high-alpine site Jungfraujoch,
637 3580 m asl, Switzerland, Atmos. Chem. Phys., 8, 5715-5729, 2008.
- 638 Stolzenburg M.R. and McMurry P.H.: TDMAFIT user's manual, University of Minnesota, Department
639 of Mechanical Engineering, Particle Technology Laboratory, Minneapolis, 1-61, 1988.
- 640 Stolzenburg M.R. and McMurry P.H.: Equations governing single and tandem DMA configurations
641 and a new lognormal approximation to the transfer function, Aerosol Sci. Tech., 42, 421-432, 2008.
- 642 Sun Y., Chen C., Zhang Y., Xu W., Zhou L., Cheng X., Zheng H., Ji D., Jie L. and Xiao T.: Rapid
643 formation and evolution of an extreme haze episode in Northern China during winter 2015, Sci.
644 Rep.-UK, 6, 2016a.
- 645 Sun Y., Wang Z., Wild O., Xu W., Chen C., Fu P., Du W., Zhou L., Zhang Q. and Han T.: "APEC
646 Blue": Secondary Aerosol Reductions from Emission Controls in Beijing., Sci. Rep.-UK, 6, 2016b.
- 647 Swietlicki E., Hansson H.C., HäMeri K., Svenningsson B., Massling A., McFiggans G., McMurry
648 P.H., PetÄJÄ T., Tunved P., Gysel M., Topping D., Weingartner E., Baltensperger U., Rissler J.,
649 Wiedensohler A. and Kulmala M.: Hygroscopic properties of submicrometer atmospheric aerosol
650 particles measured with H-TDMA instruments in various environments—a review, Tellus B, 60,
651 432-469, 10.1111/j.1600-0889.2008.00350.x, 2008.
- 652 Tan H., Liu L., Fan S., Li F., Yin Y., Cai M. and Chan P.W.: Aerosol optical properties and mixing
653 state of black carbon in the Pearl River Delta, China, Atmos. Environ., 131, 196-208,
654 10.1016/j.atmosenv.2016.02.003, 2016.
- 655 Tan H., Xu H., Wan Q., Li F., Deng X., Chan P.W., Xia D. and Yin Y.: Design and application of an
656 unattended multifunctional H-TDMA system, J. Atmos. Ocean. Tech., 30, 1136-1148, 2013a.



- 657 Tan H., Yin Y., Gu X., Li F., Chan P.W., Xu H., Deng X. and Wan Q.: An observational study of the
658 hygroscopic properties of aerosols over the Pearl River Delta region, *Atmos. Environ.*, 77, 817-826,
659 2013b.
- 660 Tao W.K., Chen J.P., Li Z., Wang C. and Zhang C.: Impact of Aerosols on Convective Clouds and
661 Precipitation, *Rev. Geophys.*, 50, 1-62, 2012.
- 662 Wang T., Nie W., Gao J., Xue L.K., Gao X.M., Wang X.F., Qiu J., Poon C.N., Meinardi S., Blake D.,
663 Wang S.L., Ding A.J., Chai F.H., Zhang Q.Z. and Wang W.X.: Air quality during the 2008 Beijing
664 Olympics: secondary pollutants and regional impact, *Atmos. Chem. Phys.*, 10, 7603-7615, 2010.
- 665 Wehner B., Berghof M., Cheng Y.F., Achtert P., Birmili W., Nowak A., Wiedensohler A., Garland
666 R.M., Pöschl U. and Hu M.: Mixing state of nonvolatile aerosol particle fractions and comparison
667 with light absorption in the polluted Beijing region, *Journal of Geophysical Research Atmospheres*,
668 114, 85-86, 2009.
- 669 Wehner B., Birmili W., Ditas F., Wu Z., Hu M., Liu X., Mao J., Sugimoto N. and Wiedensohler A.:
670 Relationships between submicrometer particulate air pollution and air mass history in Beijing, China,
671 2004-2006, *Atmos. Chem. Phys.*, 8, 6155-6168, 2008.
- 672 Wiedensohler A.: An approximation of the bipolar charge distribution for particles in the submicron
673 size range, *J. Aerosol Sci.*, 19, 387-389, 1988.
- 674 Wu G.X., Li Z.Q., Fu C.B., Zhang X.Y., Zhang R.Y., Zhang R.H., Zhou T.J., Li J.P., Li J.D. and Zhou
675 D.G.: Advances in studying interactions between aerosols and monsoon in China, *Science China*
676 *Earth Science*, 59, 1-16, 2016.
- 677 Wu Z.J., Zheng J., Shang D.J., Du Z.F., Wu Y.S., Zeng L.M., Wiedensohler A. and Hu M.: Particle
678 hygroscopicity and its link to chemical composition in the urban atmosphere of Beijing, China,
679 during summertime, *Atmos. Chem. Phys.*, 16, 1123-1138, 2016.
- 680 Zhang F., Li Y., Li Z., Sun L., Li R., Zhao C., Wang P., Sun Y., Liu X., Li J., Li P., Ren G. and Fan T.:
681 Aerosol hygroscopicity and cloud condensation nuclei activity during the AC³Exp campaign:
682 implications for cloud condensation nuclei parameterization, *Atmos. Chem. Phys.*, 14, 13423-13437,
683 10.5194/acp-14-13423-2014, 2014.
- 684 Zhang F., Li Z., Li Y., Sun Y., Wang Z., Li P., Sun L., Wang P., Cribb M., Zhao C., Fan T., Yang X.
685 and Wang Q.: Impacts of organic aerosols and its oxidation level on CCN activity from
686 measurement at a suburban site in China, *Atmos. Chem. Phys.*, 16, 5413-5425,
687 10.5194/acp-16-5413-2016, 2016.
- 688 Zhang S.L., Ma N., Kecorius S., Wang P.C., Hu M., Wang Z.B., Größ J., Wu Z.J. and Wiedensohler A.:
689 Mixing state of atmospheric particles over the North China Plain, *Atmos. Environ.*, 125, Part A,
690 152-164, 10.1016/j.atmosenv.2015.10.053, 2016.
- 691 Zhao J., Du W., Zhang Y., Wang Q., Chen C., Xu W., Han T., Wang Y., Fu P., Wang Z., Li Z. and Sun
692 Y.: Insights into aerosol chemistry during the 2015 China victory day parade: results from
693 simultaneous measurements at ground level and 260 m in Beijing, *Atmospheric Chemistry and*
694 *Physics Discussion*, published.

695

696

697



698

699 Table 1. Summary of size-resolved mean κ , the κ -PDF growth spread factor ($\sigma_{\kappa\text{-PDF}}$),
 700 size-resolved mean SF during the selected three periods, and the change in percentage
 701 of κ and SF during the control Clean1 period compared with the non-control Clean2
 702 period.

		40 nm	80 nm	110 nm	150 nm	200 nm	300 nm
Clean1	κ	0.10±0.05	0.11±0.06	0.15±0.07	0.20±0.10	0.25±0.12	—
	$\sigma_{\kappa\text{-PDF}}$	0.08±0.03	0.10±0.03	0.12±0.03	0.14±0.03	0.15±0.04	—
	SF	0.55±0.08	0.60±0.07	0.64±0.06	0.66±0.05	0.67±0.05	0.70±0.06
Clean2	κ	0.14±0.06	0.17±0.08	0.20±0.10	0.24±0.12	0.28±0.13	—
	$\sigma_{\kappa\text{-PDF}}$	0.11±0.04	0.13±0.03	0.15±0.03	0.17±0.03	0.19±0.04	—
	SF	0.60±0.06	0.66±0.07	0.70±0.07	0.72±0.07	0.74±0.06	0.78±0.06
Pollution	κ	0.16±0.08	0.24±0.08	0.30±0.09	0.36±0.10	0.42±0.12	—
	$\sigma_{\kappa\text{-PDF}}$	0.12±0.02	0.13±0.02	0.14±0.02	0.14±0.02	0.15±0.04	—
	SF	0.65±0.06	0.65±0.06	0.65±0.05	0.65±0.05	0.65±0.06	0.66±0.07
$\frac{(\text{Clean1} - \text{Clean2})}{\text{Clean2}}$	κ	-32.0%	-31.9%	-26.1%	-17.5%	-8.5%	—
	SF	-7.5%	-9.4%	-9.2%	-8.7%	-10.1%	-10.5%

703

704

705

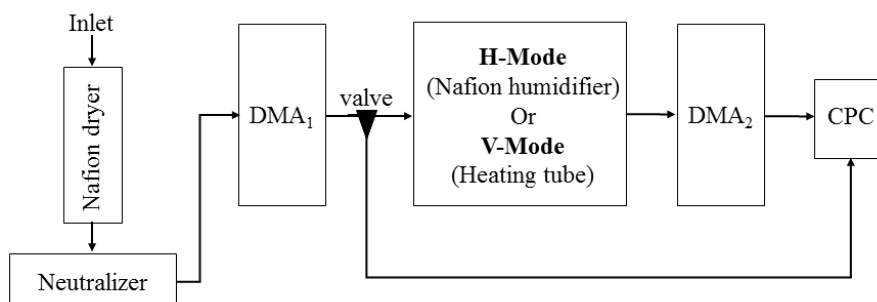


Figure 1. A schematic diagram of the hygroscopic and volatile tandem differential mobility analyzer (H/V-TDMA).

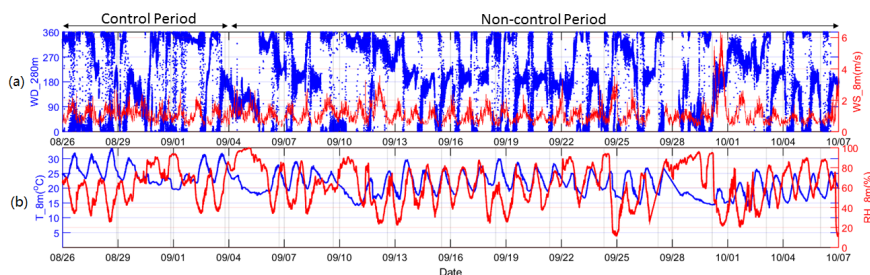
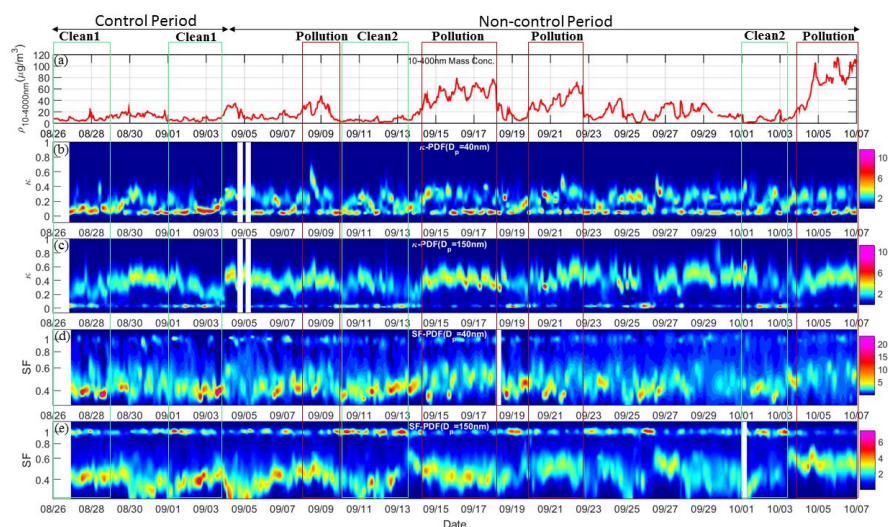


Figure 2. Time series of (a) wind direction at 280 m (in blue) and wind speed at 8 m (in red), and (b) ambient temperature at 8 m (in blue) and relative humidity at 8 m (in red) during the control and non-control periods.



715

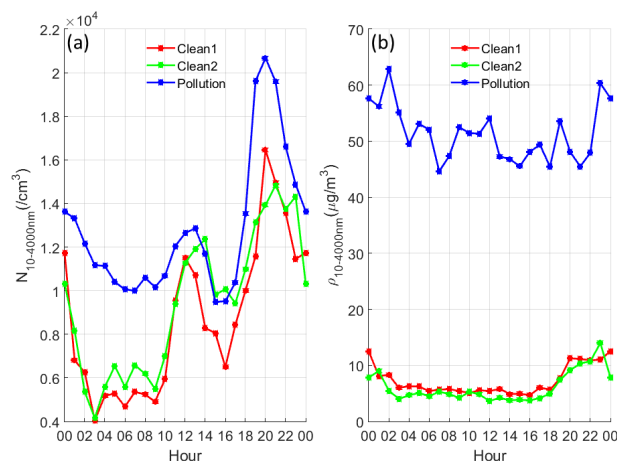
716 Figure 3. Time series of (a) 10-400 nm aerosol mass concentration ($\rho_{10-400\text{ nm}}$)

717 (assuming that the aerosol density is 1.6 g cm^{-3}), hygroscopicity parameter κ

718 distributions (κ -PDF) for (b) 40-nm and (c) 150-nm particles at RH = 90%, and

719 volatile shrink factor distributions (SF-PDF) for (d) 40-nm and (e) 150-nm particles at

720 $T = 300^\circ\text{C}$.



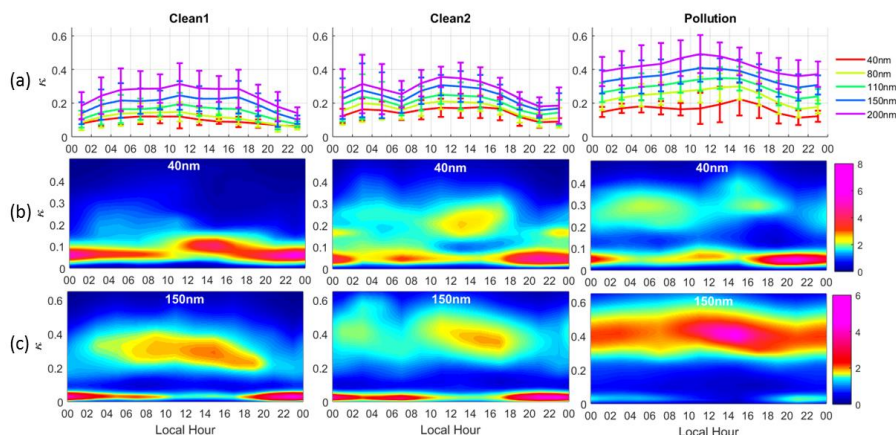
721

722 Figure 4. Diurnal variation in mobility diameter (D_p) 10-400 nm particles (a) number

723 concentration ($N_{10-400\text{ nm}}$) and (b) mass concentration ($\rho_{10-400\text{ nm}}$) for the Clean1 (in red),



724 Clean2 (in green), and Pollution (in blue) cases.

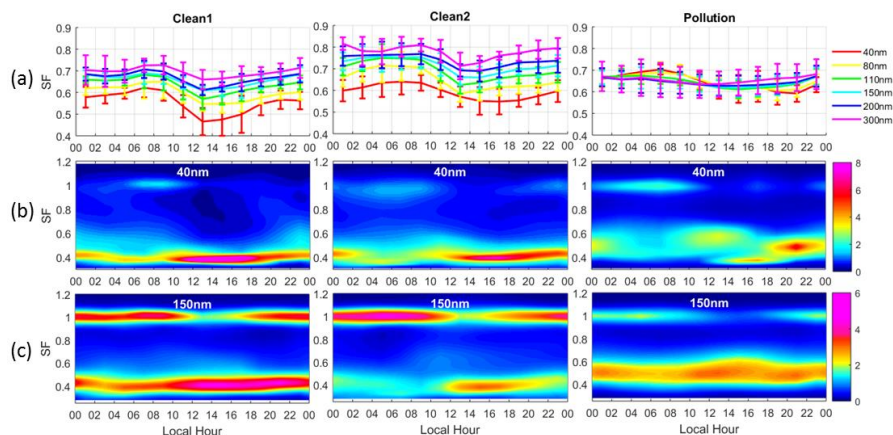


725

726 Figure 5. Diurnal variations in (a) mean κ (κ_{mean}) for different mobility diameters, (b)

727 κ -PDF for particles with D_p equal to 40 nm, and (c) κ -PDF for particles with D_p equal

728 to 150 nm during the Clean1, Clean2, and Pollution periods.



729

730 Figure 6. Diurnal variation of (a) mean SF (SF_{mean}) for different mobility diameters,

731 (b) SF-PDF for particles with D_p equal to 40 nm, and (c) SF-PDF for particles with D_p

732 equal to 150 nm during the Clean1, Clean2, and Pollution periods.

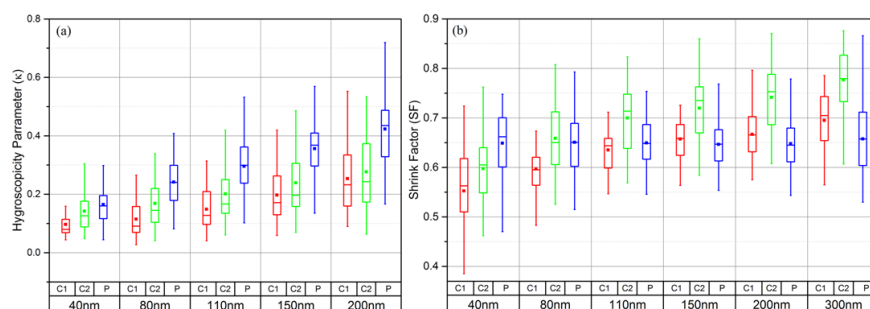


Figure 7. Size-resolved (a) κ and (b) SF during Clean1 (C1), Clean2 (C2), and Pollution (P) periods. The figure shows the mean κ or SF (solid square markers) with boxes showing the 25th, 50th, and 75th percentiles. The extremities show the 5th and 95th percentiles.

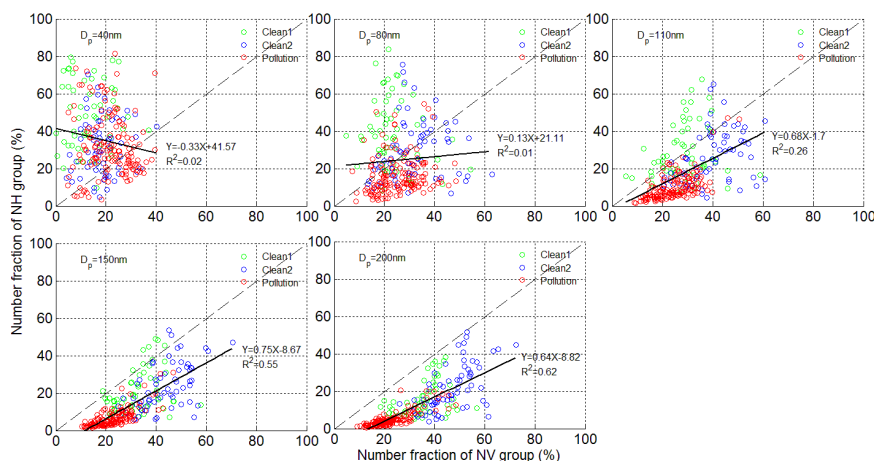


Figure 8. Comparisons between the number fractions of the nearly-hydrophobic group (NF_{NH}) and the non-volatile group (NF_{NV}) for the Clean1 (in green), Clean2 (in blue), and Pollution (in red) periods.